COMMUNICATION

Check for updates

Polyoxomolybdate-derived carbon-encapsulated multicomponent electrocatalysts for synergistically boosting hydrogen evolution†

Xiong Liu,‡[a] Kun Ni,‡[c] Bo Wen,[a] Chaojiang Niu,*[a] Jiashen Meng,[a] Ruiting Guo,[a] Qi Li,[a] Jiantao Li,[a] Yanwu Zhu, [c] Xiaojun Wu, *[b] Dongyuan Zhao [ad] and Liqiang Mai *[a]

The hydrogen adsorption strength and activity of each catalytic site greatly influence the hydrogen evolution reaction (HER) kinetics of electrocatalysts. It remains a challenge to effectively activate catalytic sites for interfacial carbon-catalyzed electrocatalysts. Here, we report a polyoxomolybdate-derived carbon-encapsulated multicomponent catalyst with nanowire structure. The activation of catalytic sites and enhancement of HER kinetics are achieved by incorporating tiny MoO_2 and Ni nanoparticles into a N-doped carbon layer (denoted as MoO_2–Ni@NC). The MoO_2–Ni@NC catalyst possesses a remarkable HER activity and is superior to most carbon-encapsulated electrocatalysts. In particular, it achieves a low overpotential of 58 mV at −10 mA cm^{-2}, and a high exchange current density of 0.375 mA cm^{-2} with good stability (up to 80 000 s) in 0.5 M H_2SO_4. Theoretical analyses suggest that the N-doped carbon layer acts as an active adsorption site for hydrogen. The inner MoO_2–Ni species behave as effective promoters to synergistically modulate the hydrogen adsorption strength on the interfacial carbon and enable the active sites to be more efficient. The synthesis strategy and the revealed catalytic mechanism can guide the rational design of high-efficiency carbon-encapsulated HER electrocatalysts.

aState Key Laboratory of Advanced Technology for Materials Synthesis and Processing, International School of Materials Science and Engineering, Wuhan University of Technology, Luoshi Road 122, Wuhan, 430070, Hubei, China. E-mail: niuchaojiang11@whut.edu.cn; mlq518@whut.edu.cn

bCAS Key Laboratory of Materials for Energy Conversion, CAS Center for Excellence in Nanoscience, Hefei National Laboratory of Physical Sciences at the Microscale, Synergetic Innovation of Quantum Information & Quantum Technology, University of Science and Technology of China, Hefei, Anhui 230026, P. R. China. E-mail: xjwu@ustc.edu.cn

cCAS Key Laboratory of Materials for Energy Conversion, Chinese Academy of Sciences, Department of Materials Science and Engineering, iChEM (Collaborative Innovation Center of Chemistry for Energy Materials), University of Science and Technology of China, 96 Jin Zhai Rd, Hefei, Anhui 230026, P. R. China

dDepartment of Chemistry, State Key Laboratory of Molecular Engineering of Polymers, Shanghai Key Laboratory of Molecular Catalysis and Innovative Materials, iChEM, Fudan University, Shanghai 200433, P. R. China

† Electronic supplementary information (ESI) available. See DOI: 10.1039/c8ta07135g

‡ These authors contributed equally to this work.

Owing to its high energy density and environmentally friendly nature, hydrogen (H_2) boosts the development of non-polluting electrocatalytic water splitting techniques for industry.[1–3] High-efficiency electrocatalysts for the hydrogen evolution reaction (HER) should be durable, active and affordable to accelerate the cathodic reaction and lower the overpotential (η) to acquire a high current density.[4] Though platinum-based materials are commonly considered as benchmark HER electrocatalysts, further scalable applications are substantially restricted by their limited reserves, high costs and instability.[5] On the other hand, as extra steps are involved in generating protons from the dissociation of water in alkaline HER processes, the electrocatalytic HER is generally faster in acidic media.[6] In recent years, numerous non-precious metal-based components (phosphides, sulfides, nitrides, borides, carbides, *etc.*) have drawn extensive attention as effective candidates.[7–12] However, harsh conditions such as strong acidic/alkaline solutions and high overpotential in electrocatalysis generally lead to corrosion or passivation of these unprotected catalysts, thus resulting in catalytic instability.[13,14] Therefore, the exploration of highly efficient and stable alternatives based on earth-abundant elements for the acidic HER is crucial.[15–17]

Due to their tunable molecular structures, superior conductivity and high resistance to chemical corrosion, carbon-based catalysts hold great potential for acidic water splitting.[18–20] However, hydrogen adsorption on the carbon surface is very weak with positive free energy of hydrogen adsorption (ΔG_{H*}, ~1.3 eV), leading to sluggish HER kinetics.[14,21] Although doping of carbon frameworks with metal-free heteroatoms (such as N, P, S, B, *etc.*) can activate the adjacent C atoms and substantially facilitate hydrogen adsorption, these derived electrocatalysts still possess large ΔG_{H*} values (>0.5 eV (ref. 22)) with unsatisfactory catalytic activity and weak comparability to precious metals.[23–26] In addition, B, P and S dopants with oxidation susceptibility at a high calcination temperature generally exhibit a poor doping efficiency in carbon materials, and thus the catalytic performances of these doped catalysts are limited.[23] Accordingly, carbon-encapsulated metal-based

catalysts have recently received extensive research interest.[27–39] Gratifyingly, carbon-encapsulated metal/alloy catalysts, as novel "chainmail" catalysts proposed by the Bao group,[13] exhibit an improved electrocatalytic activity towards the HER. The catalytic sites of such catalysts are demonstrated on the surface carbon layer. The inner metal or alloy (such as Au,[28] Co,[29] CuCo,[30] CoNi,[31] etc.) and the surface dopants can synergistically modulate the interfacial electronic states on the outermost carbon surface, thus promoting catalytic reactions. Meanwhile, with the "chainmail" structure, the outer carbon layer can protect the internal components from deactivation or dissolution. Despite this, these catalysts are still unsatisfactory with the HER η_{10} (η_{10}, which means the overpotential required to reach −10 mA cm^{-2}) usually larger than 100 mV (Fig. S1, ESI†). Very recently, carbon-encapsulated molybdenum/nickel-based electrocatalysts with platinum-like catalytic activity (η_{10} down to ∼70 mV) have attracted great interest as potential HER candidates.[38,39] And carbon-encapsulated multicomponent electrocatalysts generally possess better catalytic performance than the single-component ones.[40] In spite of these exciting improvements, complicated interactions in these multicomponent catalysts for boosting the HER are still unclear and the catalytic sites require in-depth insights. Therefore, it still remains a great challenge to rationally construct uniform carbon-encapsulated multicomponent catalysts and effectively uncover their complicated structure–performance correlations.

In this work, we propose a polyoxomolybdate-pyrolysis strategy to designedly fabricate a "chainmail" catalyst with two components confined in a carbon layer. The constructed heterogeneous nanowire arrays consist of tiny MoO_2 and Ni nanoparticles encapsulated inside the nitrogen-rich carbon layer (denoted as MoO_2–Ni@NC). After incorporating MoO_2 and Ni species into the N-doped carbon layer, the obtained MoO_2–Ni@NC catalyst possesses much lower HER overpotentials and higher exchange current density than the simplex MoO_2@NC and N-doped carbon catalysts. In particular, this novel MoO_2–Ni@NC catalyst exhibits a negligible onset potential with excellent HER activity, which is very close to that of the commercial Pt/C catalyst and superior to those of most of the reported carbon-encapsulated catalysts (Fig. S1, ESI†). On the basis of experimental and theoretical analyses, we reveal that the inner MoO_2–Ni nanoparticles synergistically modulate the electronic structure of the outer N-doped carbon layer and boost the additional interaction between the adsorbed hydrogen and C atom adjacent to the N dopant, resulting in moderate hydrogen adsorption and optimized HER activity. The deep understanding of the mechanism of the enhanced HER via incorporating multicomponent species into the carbon layer offers a promising pathway for designing high-efficiency electrocatalysts.

The MoO_2–Ni@NC nanowire arrays were fabricated via a facile polyoxomolybdate-pyrolysis method for the first time (Fig. S2, ESI†). Initially, new inorganic–organic hybrid polyoxomolybdate (denoted as MoNi-2-mim, 2-methylimidazole = 2-mim) nanowires vertically grown on carbon cloth were synthesized via a coordination reaction during solvothermal processes (Fig. 1a). Based on previous reports on its analogues,[41,42] the
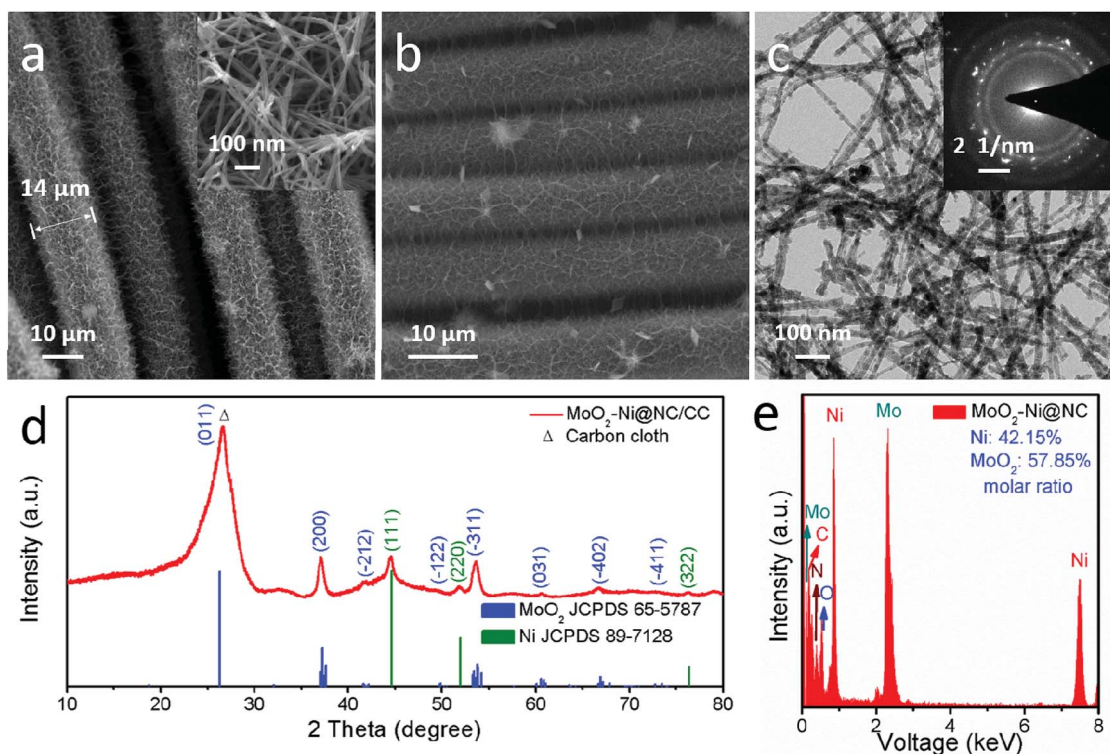

Fig. 1 (a) SEM image of MoNi-2-mim nanowire arrays. The inset in (a) is the magnified SEM image. (b) SEM image of MoO_2–Ni@NC nanowire arrays. (c) Low-magnification TEM image, (d) XRD pattern and (e) EDX spectrum of MoO_2–Ni@NC nanowires. The inset in (c) is the corresponding SAED pattern.

This journal is © The Royal Society of Chemistry 2018

J. Mater. Chem. A, 2018, 6, 17874–17881 | **17875**

2-methylimidazole coordinating nickel cation (denoted as $[Ni(2\text{-}mim)_6]^{2+}$) and 2-methylimidazole coordinating octamolybdate anion (denoted as $[(2\text{-}mim)_2Mo_8O_{26}]^{4-}$) exist in the reaction system. All the cations and anions are further joined together through complex hydrogen-bonding to form a new organic–inorganic hybrid polyoxomolybdate composite. The formation mechanism and the related characterizations of MoNi-2-mim nanowire arrays are demonstrated in detail (Fig. S3 and S4, ESI†). The MoNi-2-mim nanowires showing low-crystalline properties are several micrometers in length and have a diameter of ~20 nm. To obtain MoO_2–Ni@NC nanowire arrays, a gradient-pyrolysis strategy is applied to retain the nanowire structure. The nanowires with well-retained integrity fully cover the entire carbon cloth after calcination in Ar/H_2 (95 : 5 vol%) (Fig. 1b and S5, ESI†). The average atomic ratio of Ni/Mo in the nanowires is calculated to be about 2 : 3 by inductively coupled plasma (ICP), consistent with that of the MoNi-2-mim nanowires (Table S1, ESI†). The diameter of the obtained MoO_2–Ni@NC nanowires is ~15 nm from transmission electron microscopy (TEM) and the polycrystalline features are reflected by the selected area electron diffraction (SAED) pattern (Fig. 1c). All the MoO_2 and Ni nanoparticles are completely encapsulated inside the carbon layer, as confirmed by TEM and statistical analyses (Fig. S6, ESI†). Fig. 1d shows the MoO_2 and Ni phases (JCPDS no. 65-5787 and JCPDS no. 89-7128, respectively) of the final product, which is confirmed by the X-ray diffraction pattern (XRD). Moreover, the energy-dispersive X-ray (EDX) spectrum of MoO_2–Ni@NC nanowires demonstrates the existence of C, N, O, Ni and Mo elements (Fig. 1e).

The fine structure of MoO_2–Ni@NC nanowires has also been investigated to further illustrate the inner MoO_2, Ni nanoparticles and the outer carbon coating layer. The larger Ni nanoparticles are uniformly aligned along the axis of wires, as confirmed by TEM and high-angle annular dark-field scanning transmission electron microscopy (HAADF-STEM) images (Fig. 2a and b). STEM elemental mappings in Fig. 2c and d further demonstrate the distributions of various elements and the MoO_2–Ni species coated by the carbon layer. As shown in Fig. 2e and S6 (ESI†), there is a large Ni nanoparticle (~8 nm) closely surrounded by MoO_2 nanoparticles (~4 nm) and coated by 3–5 layers of graphitized carbon. This close contact promotes the MoO_2 and carbon species to be adequately modified by Ni nanoparticles. The interplanar spacing of 0.34 nm is assigned to the (002) lattice plane of the graphitized carbon. In the MoO_2 area, MoO_2 nanoparticles are individually embedded in the carbon layer and the outermost carbon layer is thin below 1 nm thickness (Fig. S6, ESI†). It is noted that the thicknesses of the carbon layer coated on the MoO_2 and Ni nanoparticles are clearly different, which can also be reflected by the distinct carbon distribution inside and outside of the yellow-dotted box area in Fig. 2c. Such a difference is attributed to the better catalytic ability of nickel species in the synthesis procedure, which can promote the formation of multilayer graphitized carbon and enhance the degree of graphitization (Fig. S7, ESI†).[43,44] Combined with the above-mentioned results, we therefore give the schematic illustration of MoO_2–Ni@NC as shown in Fig. 2f.

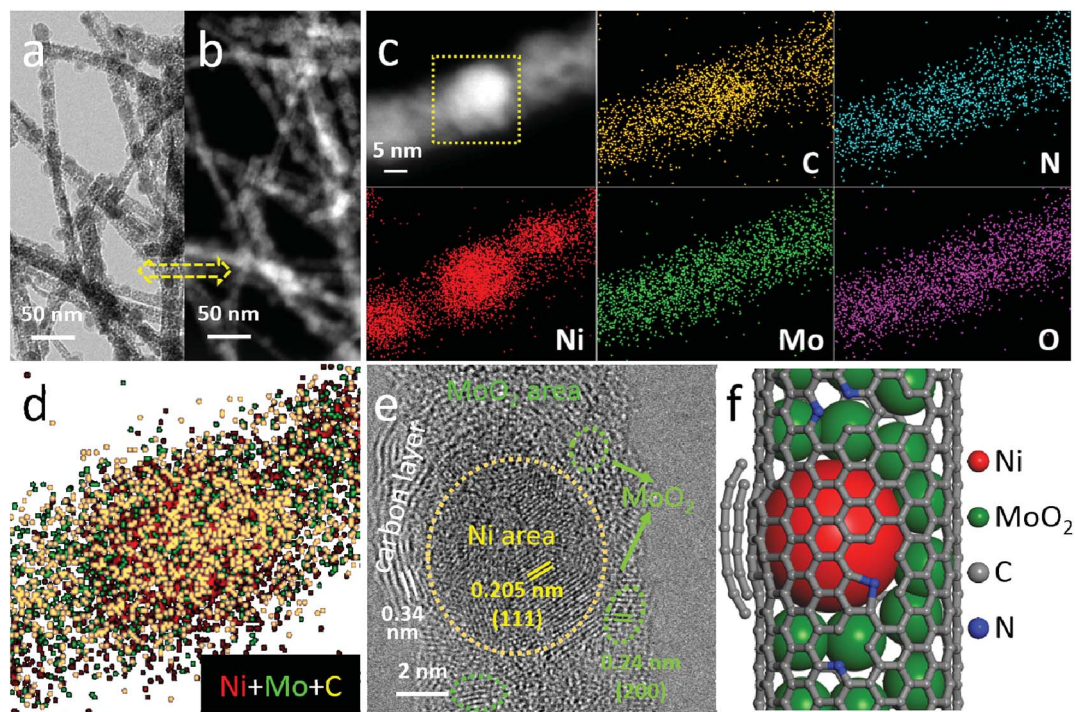The X-ray photoelectron spectra (XPS) further identify the surface states of MoO_2–Ni@NC nanowires. As shown in Fig. 3a,

Fig. 2 (a) TEM image and (b) the corresponding HAADF-STEM image of MoO_2–Ni@NC nanowires. (c) HAADF-STEM image with elemental mappings of MoO_2–Ni@NC nanowires. (d) The enlarged and mixed elemental mapping of MoO_2–Ni@NC with the black background removed. (e) High-resolution TEM image and (f) schematic illustration of MoO_2–Ni@NC.

17876 | J. Mater. Chem. A, 2018, 6, 17874–17881

This journal is © The Royal Society of Chemistry 2018
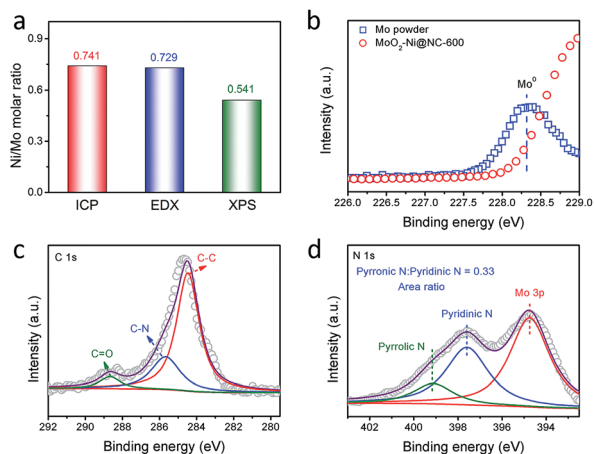
Communication

Fig. 3 (a) ICP, EDX and XPS results of the Ni/Mo molar ratios for MoO₂–Ni@NC nanowires. (b) XPS core-level spectra of Mo 3d without fitting for the Mo powder (blue) and MoO₂–Ni@NC nanowires (red). XPS core-level spectra of (c) C 1s and (d) N 1s for MoO₂–Ni@NC nanowires.

nanoparticles, which is related to the formation of graphitized carbon during calcination.[38] Fig. 3c indicates the existence of the C–N bond. The deconvolution of N 1s core level signals for MoO₂–Ni@NC nanowires further reveals peaks at 397.9 and 399.5 eV, which are assigned to the pyridinic-N and the pyrrolic-N, respectively (Fig. 3d).[45–47] Moreover, according to the CHNS results, the contents of C and N are detected as 4.17 wt% and 0.46 wt% in MoO₂–Ni@NC nanowires (Table S2, ESI†), respectively. Such a high content of the nitrogen dopant in the carbon layer is beneficial to the electrocatalytic HER as well.

A standard three-electrode system was adopted to evaluate the HER electrocatalytic activities of MoO₂–Ni@NC in 0.5 M H_2SO_4. For comparison, the MoO₂@NC and nitrogen-doped carbon (denoted as NC) were also tested as the control samples to verify the synergistic tuning between MoO₂, Ni and NC (Fig. S9–S11, ESI†). Fig. 4a shows the polarization curves of all samples in 0.5 M H_2SO_4. The MoO₂–Ni@NC displays a dramatically higher HER activity than the MoO₂@NC and NC catalysts, and it is very close to that of the commercial Pt/C. Under these conditions, the operating η_{10} values are measured to be 32 mV for Pt/C, 58 mV for MoO₂–Ni@NC, 166 mV for MoO₂@NC and 422 mV for NC according to linear scanning voltammetry (LSV) analyses. The kinetic behaviours of these catalysts are also evaluated by Tafel plots to gain more insights into the hydrogen evolution mechanism (Fig. 4b). Generally, metal-free heteroatoms (such as N, P, S, B, etc.) in carbon materials follow the Volmer–Heyrovsky pathway for the HER and the Volmer step (hydrogen adsorption on the catalyst surface) is the rate-determining step.[22,23] For our work, the Tafel slope of MoO₂–Ni@NC (35.1 mV dec⁻¹) suggests a more efficient Volmer–Tafel mechanism.[48] The smaller Tafel slope for MoO₂–Ni@NC indicates that the introduction of MoO₂ and Ni
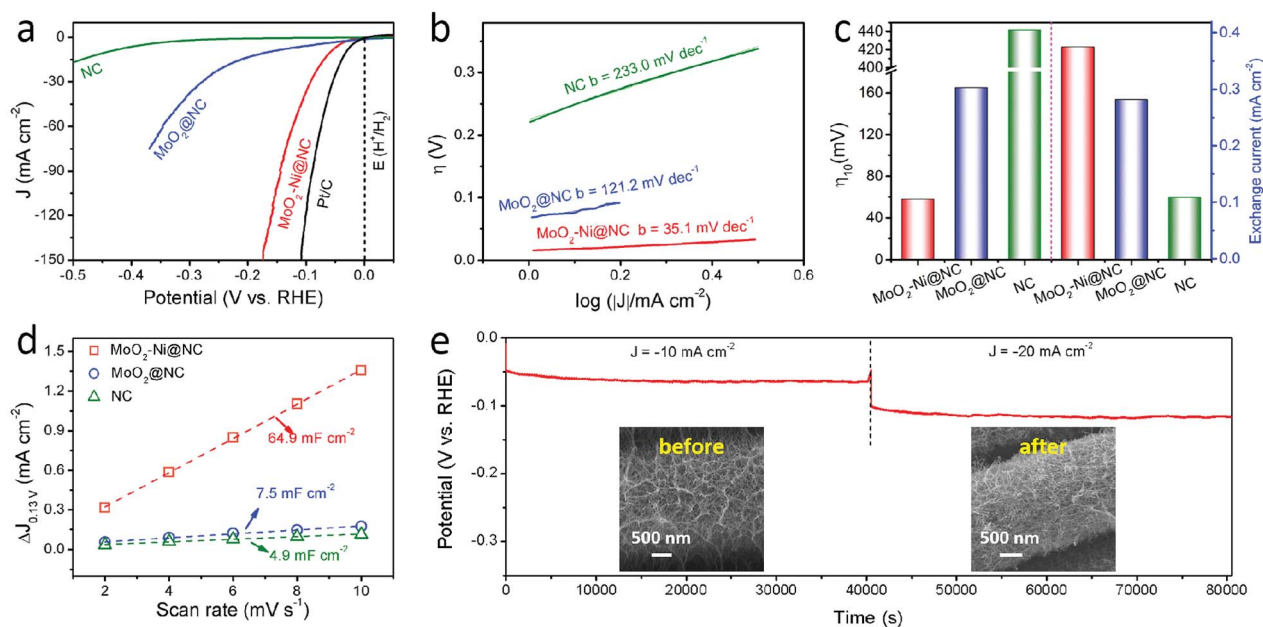
the Ni/Mo molar ratio (0.541) by XPS is smaller than the EDX result (0.729) and that determined by ICP (0.741). The different results which are attributed to the different detection depths suggest that the Ni nanoparticles are embedded more deeply underneath the outer carbon layer, consistent with the above-mentioned TEM results. No peaks for Mo⁰ species are detected, suggesting the absence of the Ni–Mo alloy (Fig. 3b).[39] In the Ni 2p region, the peaks at 853.3 and 870.6 eV belong to the metallic Ni (Fig. S8†), and the peaks at 856.2 and 874.1 eV originate from the strong Ni–C bond on the surface of Ni

Fig. 4 (a) HER polarization curves at 5 mV s⁻¹ in 0.5 M H_2SO_4. (b) Tafel plots and (c) the comparison of overpotential at −10 mA cm⁻² and exchange current density for MoO₂–Ni@NC, MoO₂@NC and NC, respectively. (d) Charging current density differences ($\Delta j = j_a - j_c$) as a function of the scan rate. (e) Galvanostatic measurements of the MoO₂–Ni@NC-600 catalyst at $j = -10$ and −20 mA cm⁻² in 0.5 M H_2SO_4. The insets are the SEM images for MoO₂–Ni@NC before and after the stability test.

can promote the hydrogen adsorption step and achieve faster catalytic kinetics. To reflect the inherent HER activity of electrocatalysts, the exchange current density (j_0) was calculated by extrapolating the Tafel plot to η at 0 V.[45] The j_0 of MoO$_2$–Ni@NC (0.375 mA cm^{-2}) is significantly larger than that of MoO$_2$@NC (0.282 mA cm^{-2}) and NC (0.108 mA cm^{-2}) (Fig. 4c).

The origins of the superior catalytic activity of MoO$_2$–Ni@NC were investigated. Firstly, the MoO$_2$–Ni@NC catalyst possesses an ultrathin nanowire structure, which is beneficial to facilitate electron transfer during the electrochemical HER process.[49,50] Electrochemical impedance spectroscopy (EIS) shows a much smaller charge transfer resistance of MoO$_2$–Ni@NC (R_{ct} value of 0.58 Ω) than that of MoO$_2$@NC (52.96 Ω), confirming a more efficient kinetic path by incorporating the Ni species (Fig. S11, ESI†). The valence band (E_v) and the improved metallic properties[51] of MoO$_2$–Ni@NC nanowires are determined from ultraviolet photoelectron spectroscopy (UPS) spectra (Fig. S13, ESI†). The MoO$_2$–Ni@NC exhibits a valence band maximum (VBM) at 2.90 eV, which is closer to the Fermi level (0 eV) than the VBM at 3.70 eV observed for MoO$_2$@NC. In order to illustrate the origin of the HER activity, the electrochemical double-layer capacitance (EDLC) was measured to evaluate the electrochemically active surface area (ECSA) of the catalysts via cyclic voltammetry (CV) measurements. The largest active surface area of MoO$_2$–Ni@NC (64.9 mF cm^{-2}) is beneficial for the best HER activity (Fig. 5d). More importantly, on the basis of the adsorption experiments,[52,53] the amount of the adsorbed protons on the MoO$_2$–Ni@NC powder is much higher than those on the MoO$_2$@NC and NC powders (Fig. S14, ESI†). The

abundant protons can accumulate on the reactive surface of MoO$_2$–Ni@NC and thus enhance the hydrogen adsorption process. Therefore, the aforementioned results indicate that synergistic regulation exists in the MoO$_2$–Ni@NC catalyst, which leads to a high-efficiency HER electrocatalysis.

As an important evaluation parameter for catalysts, the long-term durability of MoO$_2$–Ni@NC-x (x = 500, 550 or 600, corresponding to the catalysts obtained at various calcination temperatures of 500, 550 or 600 °C) was tested via galvanostatic measurements. Obviously, the MoO$_2$–Ni@NC-600 catalyst possesses the best catalytic stability with the phase structure maintained after long-term testing (Fig. 4e and S15–S17, ESI†). For instance, the potential difference ΔV_{10} ($\Delta V_{10} = V_{40\,000\,s} - V_{8\,s}$, $V_{40\,000\,s}$ and $V_{8\,s}$ mean the potential V at 40 000 s and 8 s, respectively) for MoO$_2$–Ni@NC-600 is only 39 mV, which is smaller than that of MoO$_2$–Ni@NC-550 (80 mV) and MoO$_2$–Ni@NC-500 (62 mV). The polarization curves for the MoO$_2$–Ni@NC-600 catalyst after testing for 40 000 and 80 000 s are almost overlapped with that before the testing, indicating its excellent acid-resistance. After HER testing in 0.5 M H$_2$SO$_4$ for 40 000 s, no characteristic XRD peaks of the metallic nickel are detected for MoO$_2$–Ni@NC-500 or MoO$_2$–Ni@NC-550. The disappearance of peaks indicates the massive dissolution of Ni, hence leading to rapid activity decay for these two samples. This reveals that the metallic Ni in MoO$_2$–Ni@NC nanowires is essential to achieve a high-efficiency HER. In addition, after the long-term testing, the morphology of MoO$_2$–Ni@NC-600 is almost retained with the Ni nanoparticles clearly visible. The Ni nanoparticles are incorporated into the carbon layer where the
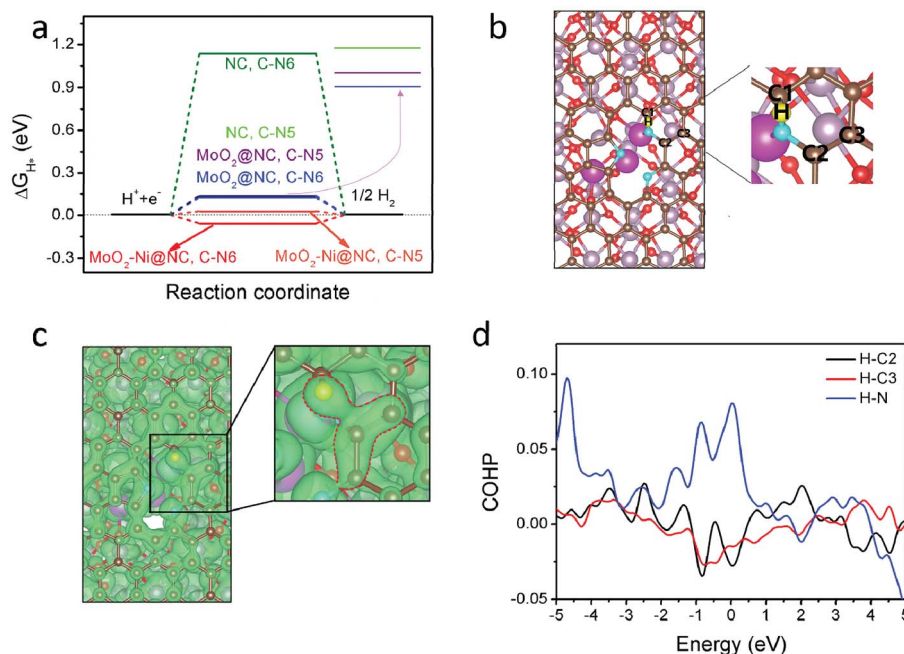

Fig. 5 (a) ΔG_{H*} calculated at the equilibrium potential of different models. The C−N5 and C−N6 refer to the C atoms bonded with the pyrrolic-N and pyridinic-N, respectively. (b) Schematic illustration of the optimal MoO$_2$–Ni@NC model with H atoms adsorbed on the C−N6 site. The C1−C3 atoms are labelled as shown in the enlarged view. The blue, brown, red, fuchsia and orchid balls refer to the N, C, O, Ni and Mo atoms, respectively. (c) Top view of the band decomposed charge density around the Fermi level. The red dashed line identifies the range of the charge density equivalent. (d) COHP analysis for the H−C2, H−C3 and H−N bonds of the MoO$_2$–Ni@NC model with H atoms adsorbed on the C−N6 site.

17878 | *J. Mater. Chem. A*, 2018, **6**, 17874–17881

This journal is © The Royal Society of Chemistry 2018

highly graphitized carbon layer plays an important role in protecting the Ni from corrosion.[13] Here, the Raman spectra of MoO_2–Ni@NC-x ($x = 500, 550, 600\ °C$) provide insights into how the calcination temperature affects the stability of Ni in the acidic solution (Fig. S7, ESI†). Two broad peaks at 1350 and 1580 cm^{-1} which are characteristic of carbon are observed for all three samples. The MoO_2–Ni@NC-600 shows the lowest I_D/I_G value, resulting in its high graphitization degree of carbon and significantly improved acid resistance. Furthermore, the higher graphitization degree of carbon can also improve the electronic conductivity,[54,55] thereby promoting the electron transfer of MoO_2–Ni@NC-600 during the HER process.

To gain insights into the HER-enhanced mechanism of MoO_2–Ni@NC, density functional theory (DFT) calculations were performed by using the Vienna Ab Initio Simulation Package (VASP) software, which is widely used to uncover the catalytic sites of electrocatalysts.[56,57] As shown in Fig. S18 and S19 (ESI)†, for the MoO_2–Ni@NC model, the active adsorption site for hydrogen is the C atom adjacent to the pyrrolic-N (denoted as the C–N5 site) and pyridinic-N (denoted as the C–N6 site) dopants, consistent with the previous reports.[35,45] In contrast, the MoO_2@NC and NC models were also established to compare the hydrogen adsorption strength on the catalyst surface (Fig. 5a). In the NC model, the positive ΔG_{H*} values of C–N5 and C–N6 sites (0.136 and 1.138 eV, respectively) indicate weak hydrogen adsorption on the N-doped carbon surfaces. And these large positive values demonstrate the inherently inferior HER activity of N-doped carbon catalysts, corresponding to the experimental results (Fig. S11c, ESI†). After introducing MoO_2, the C–N6 site is activated and the ΔG_{H*} value drops down from 1.138 to 0.125 eV, but the C–N5 sites still maintain their ΔG_{H*} value of 0.129 eV. As for the MoO_2–Ni@NC model, both the C–N5 and C–N6 sites are further activated with moderate hydrogen adsorption, suggesting their excellent HER activity. All the above calculation results are in good agreement with the observation of a significant decrease in η_{10}, the Tafel slope and j_0 after incorporating MoO_2–Ni species into the N-doped carbon-encapsulated catalyst, demonstrating the synergistic tuning between MoO_2–Ni and NC. To further reveal the above-mentioned calculation results, we also investigated the bonding nature between the adsorbed hydrogen and the interfacial N-doped carbon layer (Fig. 5b and c). The hydrogen adsorbed on the C–N6 site is discussed as an example, on which the ΔG_{H*} values gradually decrease with the introduction of MoO_2 and then Ni. In the MoO_2–Ni@NC model, the H s orbital greatly resonates with the C2 pz, C3 pz and N pz orbitals nearby the Fermi level, indicating their interactions. However, the H s orbital only resonates with the C3 pz and N pz orbitals in both MoO_2@NC and NC models (Fig. S19a–c, ESI†). To uncover the bond properties, the crystal orbital Hamilton population (COHP) calculation is applied (Fig. 5d and S20d–f, ESI†). The interactions of H–C2 and H–C3 are at a bonding state while the interaction of H–N is at an anti-bonding state. Generally, the interaction at the bonding state is beneficial for bonding strength, but that at the anti-bonding state reduces the bonding strength.[58–60] Therefore, the exclusive H–C2 bonding interaction endows the MoO_2–Ni@NC with stronger hydrogen adsorption.

In addition, the anti-bonding of H–N around the Fermi level has weakened after introducing MoO_2–Ni into NC, which is beneficial for the hydrogen adsorption of catalysts (Fig. S20f, ESI†).

Accordingly, combining the above experimental analyses and theoretical calculations, the electrocatalytic activity for the HER in our work is qualitatively stated as follows: MoO_2–Ni@NC > MoO_2@NC > NC. The catalytic origin and enhanced HER activity are attributed to the key role of MoO_2 and Ni. On one hand, the introduction of MoO_2 greatly weakens the anti-bonding of H–N, which can facilitate hydrogen adsorption. On the other hand, the introduced Ni activates the C atom at the C2 site, leading it to have a bonding interaction with the H atom that is adsorbed at the C1 site. This additional bonding further improves the hydrogen adsorption strength, resulting in greatly enhanced HER catalytic activity. Furthermore, the catalytic activity of an electrocatalyst is closely associated with its dispersity and size, and one-dimensional catalysts enable fast transportation and abundant exposed active sites.[61–63] Therefore, the ultrathin nanowire structure in MoO_2–Ni@NC with a large electrochemically active surface area also plays an important role in optimizing the electrocatalytic HER performance of the MoO_2–Ni@NC catalyst.

Conclusions

In summary, we have constructed heterogeneous nanowires containing MoO_2 and Ni nanoparticles encapsulated into a N-doped carbon layer through a polyoxomolybdate-pyrolysis method. An overpotential as low as 58 mV is required to achieve a current density of $-10\ mA\ cm^{-2}$ when the MoO_2–Ni@NC nanowire arrays are applied as the electrocatalysts for the HER in 0.5 M H_2SO_4. The introduction of MoO_2 and Ni improves the proton adsorption capability of the N-doped carbon-encapsulated catalysts, thus greatly boosting the HER process. Theoretical calculations demonstrate that the inner MoO_2–Ni species synergistically modulate the outer N-doped carbon layer and so result in enhanced HER kinetics. Further theoretical analyses reveal that MoO_2–Ni species can activate the C atoms which are bonded with pyridinic N, and the triggered additional interaction promotes moderate hydrogen adsorption and enables catalytic sites with enhanced efficiency. In addition, the highly graphitized carbon layer of MoO_2–Ni@NC nanowires protects the metallic nickel from corrosion, resulting in excellent HER stability (up to 80 000 s) in acidic media. Therefore, the obtained MoO_2–Ni@NC nanowire catalyst exhibits superior HER activity and high stability in acidic media and outperforms most carbon-encapsulated electrocatalysts reported to date. The new synthesis strategy and in-depth understanding of the catalytic mechanism may pave the way for the rational design of high-efficiency HER electrocatalysts.

Author contributions

L. M. and X. L. conceived the idea and designed the experiments. X. L., B. W., and R. G. synthesized the catalysts, performed the electrochemical experiments and analyzed the results. X. L., K. N. and X. W. performed the DFT computations

This journal is © The Royal Society of Chemistry 2018

J. Mater. Chem. A, 2018, 6, 17874–17881 | 17879

and theoretical analyses. X. L., K. N., C. N., L. M., Y. Z., D. Z. and L. M. wrote or revised the paper. All authors discussed the results and commented on the manuscript.

Conflicts of interest

There are no conflicts to declare.

Acknowledgements

Notes and references

1 D. Strmcnik, M. Uchimura, C. Wang, R. Subbaraman, N. Danilovic, V. van der, A. P. Paulikas, V. R. Stamenkovic and N. M. Markovic, *Nat. Chem.*, 2013, **5**, 300–306.
2 J. A. Turner, *Science*, 2004, **305**, 972–974.
3 Y. Zheng, Y. Jiao, Y. H. Zhu, Q. R. Cai, A. Vasileff, L. H. Li, Y. Han, Y. Chen and S.-Z. Qiao, *J. Am. Chem. Soc.*, 2017, **139**, 3336–3339.
4 J. K. Norskov and C. H. Christensen, *Science*, 2006, **312**, 1322–1323.
5 S. Cobo, J. Heidkamp, P.-A. Jacques, J. Fize, V. Fourmond, L. Guetaz, B. Jousselme, V. Ivanova, H. Dau, S. Palacin, M. Fontecave and V. Artero, *Nat. Mater.*, 2012, **11**, 802–807.
6 R. Subbaraman, D. Tripkovic, D. Strmcnik, K.-C. Chang, M. Uchimura, A. P. Paulikas, V. Stamenkovic and N. M. Markovic, *Science*, 2011, **334**, 1256–1260.
7 Y. Wang, B. Kong, D. Y. Zhao, H. T. Wang and C. Selomulya, *Nano Today*, 2017, **15**, 26–55.
8 D. Merki and X. L. Hu, *Energy Environ. Sci.*, 2011, **4**, 3878–3888.
9 W. F. Chen, J. T. Muckerman and E. Fujita, *Chem. Commun.*, 2013, **49**, 8896–8909.
10 M. Zeng and Y. G. Li, *J. Mater. Chem. A*, 2015, **3**, 14942–14962.
11 J. F. Xie and Y. Xie, *Chem.–Eur. J.*, 2016, **22**, 3588–3598.
12 M. R. Gao, Y. R. Zheng, J. Jiang and S. H. Yu, *Acc. Chem. Res.*, 2017, **50**, 2194–2204.
13 J. Deng, D. H. Deng and X. H. Bao, *Adv. Mater.*, 2017, **29**, 1606967.
14 H. B. Zhang, Z. J. Ma, J. J. Duan, H. M. Liu, G. G. Liu, T. Wang, K. Chang, M. Li, L. Shi, X. G. Meng, K. C. Wu and J. H. Ye, *ACS Nano*, 2016, **10**, 684–694.
15 J. Wang, F. Xu, H. Y. Jin, Y. Q. Chen and Y. Wang, *Adv. Mater.*, 2017, **29**, 1605838.
16 X. X. Zou and Y. Zhang, *Chem. Soc. Rev.*, 2015, **44**, 5148–5180.
17 X. Liu, B. Wen, R. T. Guo, J. S. Meng, Z. A. Liu, W. Yang, C. J. Niu, Q. Li and L. Q. Mai, *Nanoscale*, 2018, **10**, 9856–9861.
18 X. E. Liu and L. M. Dai, *Nat. Rev. Mater.*, 2016, **1**, 16064–16075.
19 Y. Zheng, Y. Jiao, Y. H. Zhu, L. H. Li, Y. Han, Y. Chen, A. J. Du, M. Jaroniec and S. Z. Qiao, *Nat. Commun.*, 2014, **5**, 3783.
20 W. J. Zhou, J. Jia, J. Lu, L. J. Yang, D. M. Hou, G. Q. Li and S. W. Chen, *Nano Energy*, 2016, **28**, 29–43.
21 J. Deng, P. J. Ren, D. H. Deng, L. Yu, F. Yang and X. H. Bao, *Energy Environ. Sci.*, 2014, **7**, 1919–1923.
22 Y. Jiao, Y. Zheng, K. Davey and S. Z. Qiao, *Nat. Energy*, 2016, **1**, 16130.
23 K. G. Qu, Y. Zheng, X. X. Zhang, K. Davey, S. Dai and S. Z. Qiao, *ACS Nano*, 2017, **11**, 7293–7300.
24 J. T. Zhang, L. T. Qu, G. Q. Shi, J. Y. Liu, J. F. Chen and L. M. Dai, *Angew. Chem., Int. Ed.*, 2016, **55**, 2230–2234.
25 Q. Han, Z. H. Cheng, J. Gao, Y. Zhao, Z. P. Zhang, L. M. Dai and L. T. Qu, *Adv. Funct. Mater.*, 2017, **27**, 1606352.
26 Y. C. Zhou, Y. H. Leng, W. J. Zhou, J. L. Huang, M. W. Zhao, J. Zhan, C. H. Feng, Z. H. Tang, S. W. Chen and H. Liu, *Nano Energy*, 2015, **16**, 357–366.
27 Y. Hou, Z. H. Wen, S. M. Cui, S. Q. Ci, S. Mao and J. H. Chen, *Adv. Funct. Mater.*, 2015, **25**, 872–882.
28 W. J. Zhou, T. L. Xiong, C. H. Shi, J. Zhou, K. Zhou, N. W. Zhu, L. G. Li, Z. H. Tang and S. W. Chen, *Angew. Chem., Int. Ed.*, 2016, **128**, 8556–8560.
29 X. X. Zou, X. X. Huang, A. Goswami, R. Silva, B. R. Sathe, E. Mikmekova and T. Asefa, *Angew. Chem., Int. Ed.*, 2014, **126**, 4461–4465.
30 M. Kuang, Q. H. Wang, P. Han and G. F. Zheng, *Adv. Energy Mater.*, 2017, **7**, 1700193.
31 J. Deng, P. J. Ren, D. H. Deng and X. H. Bao, *Angew. Chem., Int. Ed.*, 2015, **54**, 2100–2104.
32 W. J. Zhou, J. Zhou, Y. C. Zhou, J. Lu, K. Zhou, L. J. Yang, Z. H. Tang, L. G. Li and S. W. Chen, *Chem. Mater.*, 2015, **27**, 2026–2032.
33 M. Tavakkoli, T. Kallio, O. Reynaud, A. G. Nasibulin, C. Johans, J. Sainio, H. Jiang, E. I. Kauppinen and K. Laasonen, *Angew. Chem., Int. Ed.*, 2015, **54**, 4535–4538.
34 S. H. Noh, M. H. Seo, J. Kang, T. Okajima, B. Han and T. Ohsaka, *NPG Asia Mater.*, 2016, **8**, e312.
35 Y. Yang, Z. Y. Lun, G. L. Xia, F. C. Zheng, M. N. He and Q. W. Chen, *Energy Environ. Sci.*, 2015, **8**, 3563–3571.
36 Y. T. Xu, X. F. Xiao, Z. M. Ye, S. L. Zhao, R. A. Shen, C. T. He, J. P. Zhang, Y. D. Li and X. M. Chen, *J. Am. Chem. Soc.*, 2017, **139**, 5285–5288.
37 D. Y. Chung, S. W. Jun, G. Yoon, H. Kim, J. M. Yoo, K.-S. Lee, T. Kim, H. Shin, A. K. Sinha, S. G. Kwon, K. Kang, T. Hyeon and Y.-E. Sung, *J. Am. Chem. Soc.*, 2017, **139**, 6669–6674.
38 S. P. Wang, J. Wang, M. L. Zhu, X. B. Bao, B. Y. Xiao, D. F. Su, H. R. Li and Y. Wang, *J. Am. Chem. Soc.*, 2015, **137**, 15753–15759.
39 T. Wang, Y. R. Guo, Z. X. Zhou, X. H. Chang, J. Zheng and X. G. Li, *ACS Nano*, 2016, **10**, 10397–10403.
40 Y. X. Lin, L. Yang, Y. K. Zhang, H. L. Jiang, Z. J. Xiao, C. Q. Wu, G. B. Zhang, J. Jiang and L. Song, *Adv. Energy Mater.*, 2018, **8**, 1703623.

17880 | *J. Mater. Chem. A*, 2018, **6**, 17874–17881

This journal is © The Royal Society of Chemistry 2018

41 C. H. Tian, Z. G. Sun, J. Li, X. F. Zheng, H. D. Liang, L. C. Zhang, W. S. You and Z. M. Zhu, *Inorg. Chem. Commun.*, 2007, **10**, 757–761.

42 M. L. Cao and X. L. Zhang, *J. Mol. Struct.*, 2011, **994**, 75–81.

43 Y. Xu, W. G. Tu, B. W. Zhang, S. M. Yin, Y. Z. Huang, M. Kraft and R. Xu, *Adv. Mater.*, 2017, **29**, 1605957.

44 J. S. Meng, C. J. Niu, L. H. Xu, J. T. Li, X. Liu, X. P. Wang, Y. Z. Wu, X. M. Xu, W. Y. Chen, Q. Li, Z. Z. Zhu, D. Y. Zhao and L. Q. Mai, *J. Am. Chem. Soc.*, 2017, **139**, 8212–8221.

45 J. W. Su, Y. Yang, G. L. Xia, J. T. Chen, P. Jiang and Q. W. Chen, *Nat. Commun.*, 2017, **8**, 14969.

46 Y. C. Hao, Y. Q. Xu, W. Liu and X. M. Sun, *Mater. Horiz.*, 2018, **5**, 108–115.

47 Z. X. Song, W. W. Liu, N. C. Cheng, M. N. Banis, X. Li, Q. Sun, B. W. Xiao, Y. L. Liu, A. Lushington, R. Y. Li, L. M. Liu and X. L. Sun, *Mater. Horiz.*, 2017, **4**, 900–907.

48 R. Zhang, X. X. Wang, S. J. Yu, T. Wen, X. W. Zhu, F. X. Yang, X. N. Sun, X. K. Wang and W. P. Hu, *Adv. Mater.*, 2017, **29**, 1605502.

49 L. Liao, S. N. Wang, J. J. Xiao, X. J. Bian, Y. H. Zhang, M. D. Scanlon, X. L. Hu, B. H. Liu and H. H. Girault, *Energy Environ. Sci.*, 2014, **7**, 387–392.

50 Q. P. Lu, A. L. Wang, Y. Gong, W. Hao, H. F. Cheng, J. Z. Chen, B. Li, N. L. Yang, W. X. Niu, J. Wang, Y. F. Yu, X. Zhang, Y. Chen, Z. X. Fan, X. J. Wu, J. P. Chen, J. Luo, S. Z. Li, L. Gu and H. Zhang, *Nat. Chem.*, 2018, **10**, 456–461.

51 M. A. Lukowski, A. S. Daniel, C. R. English, F. Meng, A. Forticaux, R. J. Hamers and S. Jin, *Energy Environ. Sci.*, 2014, **7**, 2608–2613.

52 H. Li, W. Q. Kong, J. Liu, N. Y. Liu, H. Huang, Y. Liu and Z. H. Kang, *Carbon*, 2015, **91**, 66–75.

53 Y. Y. Ma, C. X. Wu, X. J. Feng, H. Q. Tan, L. K. Yan, Y. Liu, Z. H. Kang, E. B. Wang and Y. G. Li, *Energy Environ. Sci.*, 2017, **10**, 788–798.

54 J. S. Meng, X. Liu, J. T. Li, Q. Li, C. Zhao, L. H. Xu, X. P. Wang, F. Liu, W. Yang, X. M. Xu, Z. A. Liu, C. J. Niu and L. Q. Mai, *Nano Lett.*, 2017, **17**, 7773–7781.

55 H. Wang, S. X. Min, C. Ma, Z. X. Liu, W. Y. Zhang, Q. Wang, D. B. Li, Y. Y. Li, S. Turner, Y. Han, H. B. Zhu, E. Abouhamad, M. N. Hedhili, J. Pan, W. L. Yu, K.-W. Huang, L.-J. Li, J. Y. Yuan, M. Antonietti and T. Wu, *Nat. Commun.*, 2017, **8**, 13592.

56 J. Hafner, *J. Comput. Chem.*, 2008, **29**, 2044–2078.

57 H. Y. Jin, C. X. Guo, X. Liu, J. L. Liu, A. Vasileff, Y. Jiao, Y. Zheng and S.-Z. Qiao, *Chem. Rev.*, 2018, **118**, 6337–6408.

58 R. Dronskowski and P. E. Blöchl, *J. Phys. Chem.*, 1993, **97**, 8617–8624.

59 V. L. Deringer, A. L. Tchougréeff and R. Dronskowski, *J. Phys. Chem. A*, 2011, **115**, 5461–5466.

60 V. L. Deringer, U. Englert and R. Dronskowski, *Chem. Commun.*, 2014, **50**, 11547–11549.

61 L. M. Zhou, J. Meng, P. Li, Z. L. Tao, L. Q. Mai and J. Chen, *Mater. Horiz.*, 2017, **4**, 268–273.

62 Y. L. Zhu, W. Zhou, Y. J. Zhong, Y. F. Bu, X. Y. Chen, Q. Zhong, M. L. Liu and Z. P. Shao, *Adv. Energy Mater.*, 2017, **7**, 1602122.

63 Y. N. Chen, S. M. Xu, Y. C. Li, R. J. Jacob, Y. D. Kuang, B. Y. Liu, Y. L. Wang, G. Pastel, L. G. Salamanca-Riba, M. R. Zachariah and L. B. Hu, *Adv. Energy Mater.*, 2017, **7**, 1700482.